

LETTER TO THE EDITOR

MeV absorption in gamma-ray bursts as a probe of their progenitor winds

Gor Oganesyan^{1,2,3*}, Om Sharan Salafia^{4,5**}, Emanuele Sobacchi^{1,2***}, Samanta Macera^{1,2}, Giancarlo Ghirlanda^{4,5}, Lara Nava^{4,6}, Annarita Ierardi^{1,2}, Biswajit Banerjee^{1,2}, Alessio Mei⁴, Stefano Ascenzi^{1,2}, and Marica Branchesi^{1,2,3}

¹ Gran Sasso Science Institute, Viale F. Crispi 7, L’Aquila (AQ), I-67100, Italy

² INFN - Laboratori Nazionali del Gran Sasso, L’Aquila (AQ), I-67100, Italy

³ INAF - Osservatorio Astronomico d’Abruzzo, Via M. Maggini snc, I-64100 Teramo, Italy

⁴ INAF - Osservatorio Astronomico di Brera, via E. Bianchi 46, I23807 Merate (LC), Italy

⁵ INFN – Sezione di Milano-Bicocca, Piazza della Scienza 3, 20146, Milano (MI), Italy

⁶ INFN, Sezione di Trieste, I-34127 Trieste, Italy

Received xxx; accepted xxx

ABSTRACT

A small fraction of X-ray photons from γ -ray bursts (GRBs), after escaping the relativistic jet, are scattered by electrons in the circumburst medium. Subsequent photon–photon absorption between the incoming MeV γ -rays and the back-scattered X-rays generate electron–positron pairs, enriching the surrounding medium with leptons. We investigate how these back-scattered photons modify the prompt GRB spectrum through $\gamma - \gamma$ absorption. In a dense and pair-loaded wind environment, the emerging spectra exhibit a broad attenuation structure, whose morphology is sensitive to the low-energy spectral index α . In particular, spectra with $\alpha > -1$ develop a pronounced, saddle-shaped absorption between 1 and 100 MeV (rest frame). Such external MeV absorption could account for the spectral curvature seen in some bright GRBs, and may point to enhanced mass loss from their progenitor stars—consistent with early observations of core-collapse supernovae.

Key words. Gamma-ray burst: general – radiation mechanisms: non-thermal – Methods: analytical – Methods: data analysis – Methods: miscellaneous

1. Introduction

Gamma-ray bursts (GRBs) are brief (\sim 0.1–100 s) extragalactic transients releasing enormous energies of 10^{52} – 10^{54} erg, predominantly observed in the keV–MeV range. A fraction of the prompt GRB photons, after escaping the relativistic jet where they are produced, are Thomson-scattered by cold electrons in the circumburst medium. The interaction between these back-scattered X-ray photons and the incoming MeV γ -rays leads to $\gamma - \gamma$ absorption and the subsequent creation of electron–positron pairs, which further enhance the scattering rate. Consequently, the immediate environment of the burst becomes enriched with pairs (Thompson & Madau 2000; Mészáros et al. 2001; Beloborodov 2002). Continuous momentum deposition by the prompt emission photons accelerates this pair-enriched layer to ultra-relativistic velocities (Madau & Thompson 2000; Beloborodov 2002).

The influence of pair-loading on the early afterglow emission has been extensively studied (Mészáros et al. 2001; Beloborodov 2002; Kumar & Panaiteescu 2004; Beloborodov 2005; Ramirez-Ruiz et al. 2007; Ghisellini et al. 2010; Nava et al. 2013). However, its possible feedback on the prompt emission itself has received little attention. The enhanced lepton density could, in

principle, cause significant absorption of MeV γ -rays by previously back-scattered X-ray photons via $\gamma - \gamma$ absorption. As noted by Mészáros et al. (2001) and Beloborodov (2002), such absorption features are expected to be most prominent in wind-like external media, where the high densities of free electrons at radii $\gtrsim 10^{13}$ – 10^{14} cm coincide with the region of prompt emission.

In this Letter, we investigate spectral absorption features in GRB prompt emission induced by X-ray photons scattered by the circumburst medium. We develop a semi-analytical model that self-consistently includes Thomson scattering, $\gamma - \gamma$ absorption, and the resulting pair-loading (Section 2). We then apply this model to the prompt emission spectrum of GRB 190114C (Section 3) to constrain the velocity of the wind and the mass-loss rate of its progenitor star. The broader implications of our results are discussed in Section 4, followed by our conclusions in Section 5.

Hereafter, we adopt the notation $Q = 10^x Q_x$, and cgs units unless otherwise specified, and a flat Cosmology with Λ CDM parameters from Planck Collaboration et al. (2016).

2. The Model

The basic concept of external MeV absorption is illustrated in Fig. 1. The GRB spectrum is assumed to be a peaked function in the νL_ν representation (erg s^{-1}), with a low-energy slope corresponding to the single-electron synchrotron spectrum below the peak energy E_p (left-hand panels). Our choice of the low-energy slope is motivated by the findings of Oganesyan et al. (2017) and

* e-mail: gor.oganesyan@gssi.it

** e-mail: om.salafia@inaf.it

*** e-mail: emanuele.sobacchi@gssi.it

¹ The role of pair-enrichment by compact MeV sources has been first discussed in the context of Active Galactic Nuclei by Guilbert et al. (1983) and Beloborodov (1999).

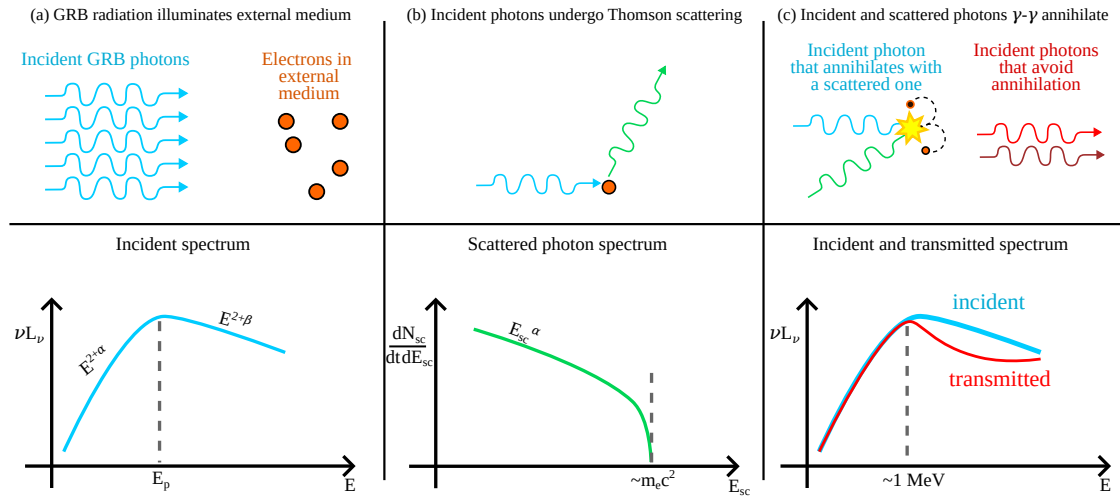


Fig. 1. Sketch of the process that leads to the absorption feature that we discuss in this work. (a) The radiation from the GRB jet illuminates some external material located at a radius R_0 . (b) Some of the photons in the incident GRB radiation undergo Thomson scattering off the electrons in the external medium. Because of the Klein-Nishina suppression of the Thomson cross section, the spectrum of the scattered photon spectrum cuts off at a photon energy $E_{sc} \sim m_e c^2$. (c) Incident photons above a threshold energy $E \gtrsim 2.5 m_e c^2$ can annihilate with the scattered photons, leaving an absorption feature in the transmitted spectrum. If the low-energy photon index in the incident spectrum satisfies $\alpha > -1$, then the feature is saddle-shaped.

Ravasio et al. (2018, 2019a, see also Toffano et al. 2021), and we note that the median low-energy photon index of the brightest GRB spectra, modeled by the Band function, is -0.64 (Gruuber et al. 2014). A fraction of GRB photons undergo Thomson scattering on cold electrons in the circum-burst medium, producing a population of scattered photons (central panel). The rate of scattered photons per unit solid angle is determined by the differential Klein-Nishina cross section, with the characteristic energy $E_{max} \approx 0.4 m_e c^2$. These scattered photons can then annihilate with the incoming MeV photons via $\gamma\gamma$ pair production (Madau & Thompson 2000, right-hand panel).

Because of the $\gamma\gamma$ absorption threshold, this process becomes relevant only for incident photon energies above $E \approx 2.5 m_e c^2/(1+z)$ in the observer frame, where z is the redshift of the source. In the illustrative case considered here, with $\nu L_\nu \propto E^{2+\alpha}$ below the peak energy, and with $\alpha > -1$, the absorption weakens at the highest energies, producing a saddle-shaped absorption in the MeV range. This behavior arises because the number density of the scattered photons increases with energy. In contrast, spectra with $\alpha \leq -1$ would exhibit a sharp suppression of all MeV photons above $2.5 m_e c^2/(1+z)$ (see Appendix A.4). Hence, the low-energy photon index α has a central role in determining the detailed shape of the MeV absorption feature.

To quantify this picture, we consider a burst of un-polarised MeV radiation of a finite duration produced in a relativistic jet at a distance R_γ from the central engine. We estimate the fate of the first photons escaping the jet and scattering off cold electrons in the circum-burst medium. At a distance $R > R_\gamma$, an electron scatters the incoming photons at an average rate

$$\frac{dN_{sc}}{dt} \sim \frac{L \sigma_T}{4\pi R^2 m_e c^2}, \quad (1)$$

where L is the isotropic-equivalent luminosity of the MeV front. The scattered photons have a typical survival time against $\gamma\gamma$ absorption, as measured in the central engine rest frame, of

$$\frac{\lambda_{\gamma\gamma}}{c} \sim \frac{4\pi R^2 m_e c^2}{\eta \sigma_T L}, \quad (2)$$

where σ_T is the Thomson cross section, and $\eta \sigma_T$ is the peak value of the $\gamma\gamma$ cross section, with $\eta \sim 1/5$ (Svensson 1987).

For representative values of R and L , one finds $\lambda_{\gamma\gamma}/c \sim 8 \times 10^{-4} R_{15}^2 L_{53}^{-1}$ s which, sufficiently close to the GRB emission site, is shorter than both the burst duration and its variability timescale.

The optical depth to $\gamma\gamma$ absorption for MeV photons that travel through the scattered X-ray photons can therefore be estimated (see Appendix A.3 for a detailed treatment)

$$\tau_{\gamma\gamma} \sim Z_\pm \hat{n}(R_0) R_0 \eta \sigma_T \frac{dN_{sc}}{dt} \frac{\lambda_{\gamma\gamma}}{c} \sim Z_\pm \hat{n}(R_0) R_0 \sigma_T, \quad (3)$$

where $\hat{n}(R_0)$ is the number density of the external medium, Z_\pm is the lepton enhancement factor due to pair loading, and R_0 is the distance from the central engine where the dominant absorption takes place. This immediately shows that the absorption can be relevant (that is, $\tau_{\gamma\gamma} \gtrsim 1$) if the external density of leptons (after pair loading) is as high as

$$Z_\pm \hat{n}(R_0) \gtrsim 1.5 \times 10^9 R_{0,15}^{-1} \text{ cm}^{-3}. \quad (4)$$

If we assume a wind-like profile for the external medium, and we write $\hat{n}(R) = \hat{A}_*(R/5.5 \times 10^{17} \text{ cm})^{-2}$ (so that $\hat{A}_* = 1 \text{ cm}^{-3}$ corresponds to the density of a stellar wind with a mass loss rate $\dot{M} = 10^{-5} M_\odot \text{ yr}^{-1}$ and a velocity $v_w = 10^3 \text{ km s}^{-1}$, typical of a Wolf-Rayet star – Chevalier & Li 1999), then this translates to

$$Z_\pm \hat{A}_* \gtrsim 5 \times 10^3 R_{0,15} \text{ cm}^{-3}. \quad (5)$$

In a wind-like circum-burst medium, most of the optical depth of this process is provided by the innermost layers, closest to R_γ . The scattering and pair enrichment of the medium, though, can accelerate these inner layers, inflating a cavity (Madau & Thompson 2000; Beloborodov 2002): at a rest-frame time t since the start of the prompt emission, the absorption is therefore mainly provided by the inner radius of the cavity, where the circum-burst medium has been loaded with pairs, but not yet accelerated. This corresponds to a radius (Beloborodov 2005, see also Appendix A.4)

$$R_0(t) \sim 7.9 \times 10^{15} L_{53}^{1/2} t_0^{1/2} \xi_{acc,2}^{-1/2} \text{ cm}, \quad (6)$$

where $\xi_{\text{acc}} \sim 100-150$ is a dimensionless parameter that depends on the shape of the incident spectrum, and L here must be interpreted as the average luminosity until time t . At that radius, the pair-loading factor of the material that has not been accelerated yet by the prompt emission photons is $Z_{\pm} \sim 74$ (Beloborodov 2002). The minimum required wind parameter for absorption effects to be relevant therefore becomes

$$\hat{A}_{\star} \gtrsim 5.3 \times 10^2 L_{53}^{1/2} t_0^{1/2} \xi_{\text{acc},2}^{-1/2} \text{ cm}^{-3}. \quad (7)$$

For soft GRB spectra ($\alpha < -1$; see Fig. A.3), the absorption produces a cut-off at high energy, which is visible already with $\hat{A}_{\star} \gtrsim \text{few} \times 100 \text{ cm}^{-3}$. For harder GRB spectra ($\alpha > -1$) and $\hat{A}_{\star} \gtrsim 1000 \text{ cm}^{-3}$, a saddle-shaped absorption feature becomes visible.

Because $\tau_{\gamma\gamma}$ and the Thomson optical depth $\tau_{\gamma e}$ are of comparable magnitude, the MeV absorption should be accompanied by a corresponding reduction of X-ray photons due to Thomson scattering by the same pair-enriched leptons. An accurate model that accounts for the detailed pair-loading profile is presented in Appendix A.

3. GRB 190114C as a test case

Among the population of bright GRBs with well-sampled MeV coverage, we selected GRB 190114C, for which independent analyses have reported a sharp spectral cutoff around ~ 1 MeV, followed by a nearly flat spectrum up to ~ 100 MeV (Ajello et al. 2020; Macera et al. 2025). We analysed the early-time emission (0–4.15 s) of GRB 190114C by combining data from the *Fermi* Gamma-ray Burst Monitor (GBM; 8 keV–40 MeV) and the Large Area Telescope Low-Energy (LAT-LLE) data set (30–100 MeV). The spectrum was initially fitted with the empirical Band function (Band et al. 1993), defined by four free parameters: the low- and high-energy photon indices α and β , the peak energy E_p , and a normalisation constant. While the Band model reproduces the sub-MeV portion of the spectrum (< 1 MeV) well, it fails to account for the pronounced curvature in the 1–100 MeV range (left panel of Fig. 2). The residuals reveal a broad, saddle-shaped deviation across this energy band.

To test the external absorption scenario, we implemented a custom model for the X-ray spectral fitting package XSPEC (Arnaud 1996). The model assumes $t_0 = 4.15 \text{ s}/(1+z) \approx 2.9 \text{ s}$ and has five free parameters: the low ($-1.5 < \alpha < -0.3$) and high-energy photon index ($-2.5 < \beta < -2.0$), the spectral peak ($2.5 < \log_{10}(E_p/\text{keV}) < 4.0$), the wind-density normalisation ($2 < \log_{10}(\hat{A}_{\star}/\text{cm}^{-3}) < 5$), and the unabsorbed bolometric luminosity ($50 < \log_{10}(L/\text{erg s}^{-1}) < 55$). The absorption radius R_0 is computed according to Eq. 6, keeping $\xi_{\text{acc}} = 100$ fixed for simplicity. For the absorbed Band model, the redshift of GRB 190114C is fixed at $z = 0.4245$ (Castro-Tirado et al. 2019).

Table B.1 lists the best-fit parameters for both the Band and absorbed Band models, while Fig. 2 shows the corresponding νF_{ν} spectrum. Incorporating $\gamma\gamma$ absorption improves the fit (right panel of Fig. 2), with $\Delta_{\text{stat}} = 147$ for one additional parameter (\hat{A}_{\star}). This provides strong evidence that external absorption may play a significant role in shaping the prompt MeV spectrum of GRB 190114C. The best-fit density is $A_{\star} \approx 10^4 \text{ cm}^{-3}$, while the luminosity is $L \approx 3.5 \times 10^{53} \text{ erg s}^{-1}$, which yields an absorption radius of $R_0 \approx 2.5 \times 10^{16} \text{ cm}$.

4. Discussion

4.1. Implications for the progenitor winds

The wind density is determined by the progenitor's mass-loss rate \dot{M} and wind velocity v_w prior to core collapse (Chevalier & Li 1999) as $\hat{n}(R) = \dot{M}/4\pi m_p v_w R^2$, which leads to the definition $\hat{A}_{\star} = \dot{M}_{-5} v_{w,3}^{-1} \text{ cm}^{-3}$, with \dot{M} expressed in $\text{M}_{\odot} \text{ yr}^{-1}$ and v_w in km s^{-1} . Long GRBs are generally believed to be associated with Wolf-Rayet progenitors (Woosley 1993; Woosley & Bloom 2006), whose mass-loss rates are highly uncertain, ranging from $\dot{M} \sim 10^{-5} \text{ M}_{\odot} \text{ yr}^{-1}$ up to $\sim 10^{-3} \text{ M}_{\odot} \text{ yr}^{-1}$, with velocities between a few hundreds up to thousands of km s^{-1} (e.g. Vink & de Koter 2005; Vink et al. 2011; Sander et al. 2023; Pauli et al. 2025). $A_{\star} = 1 \text{ cm}^{-3}$ hence corresponds to fiducial parameters, but there is in principle ample space for variation around this value, which could accommodate the very high value found here for GRB 190114C.

The wind normalization parameter is commonly inferred from GRB afterglow modeling, as the emission arises from a relativistic shock running into the circum-burst medium (Mészáros & Rees 1997). Although individual estimates vary widely, typical results suggest $\hat{A}_{\star} \lesssim 0.1 - 1$ (Panaiteescu & Kumar 2002; Beniamini et al. 2015; Tiwari et al. 2025). However, there is growing evidence that some progenitors undergo enhanced mass loss in the years preceding core collapse (e.g. Schlegel 1990; Chugai & Danziger 2003; Chugai et al. 2004; Campana et al. 2006; P astorello et al. 2007; Kiewe et al. 2012; Ofek et al. 2014; Groh 2014; Khazov et al. 2016; Yaron et al. 2017, see also Salafia et al. 2026 on GRB 221009A), reaching up to $\dot{M} \sim 10^{-1} \text{ M}_{\odot} \text{ yr}^{-1}$. Such late-stage wind enhancement would increase the density of the circum-burst medium only in the immediate vicinity of the progenitor, at radii $R \approx 3 \times 10^{15} T_{\text{yr}} v_{w,3} \text{ cm}$, where T_{yr} is the time, in units of years, during which the enhanced mass loss has taken place before core collapse. Consequently, the afterglow emission – produced at much larger radii – would be largely insensitive to this late mass-loss episode, whereas the MeV absorption during the prompt phase could directly probe it.

4.2. Absorption site and jet bulk Lorentz factor

Modeling of the spectrum of GRB 190114C indicates an absorption region of characteristic size $R_0 \approx 2.5 \times 10^{16} \text{ cm}$. For backscattering and subsequent $\gamma\gamma$ absorption to occur, the prompt emission photons must first escape the relativistic jet in which they are produced. The width of the radiation front emerging from the jet is $\Delta_{\gamma} \approx R_{\gamma} + R/2\Gamma^2$, where Γ is the bulk Lorentz factor of the jet. In the case of GRB 190114C, this width must be $\Delta_{\gamma} \gtrsim ct$, where $t \sim 4.15/(1+z) = 2.9 \text{ s}$, otherwise the jet would collide with the absorption region and accelerate it before the absorption could take place. This implies an upper limit on the jet bulk Lorentz factor, $\Gamma \lesssim 400 R_{16.4}^{1/2} t_{0.46}^{-1/2}$ (assuming $R_{\gamma} \ll R_0$). This estimate is in agreement with that proposed by Derishev & Piran (2019) based on the requirement of transparency of the blastwave to TeV photons in the early afterglow. When accounting for the high external medium density, it is also consistent with estimates derived from the time of the onset of the afterglow (Ravasio et al. 2019b; MAGIC Collaboration et al. 2019).

4.3. Relevance to the observed prompt emission features

If the wind density requirements are met, the spectra of collapse-driven GRBs are expected to exhibit absorption of MeV γ -rays above $2.5 m_e c^2$ in the rest frame. The detailed shape of this ab-

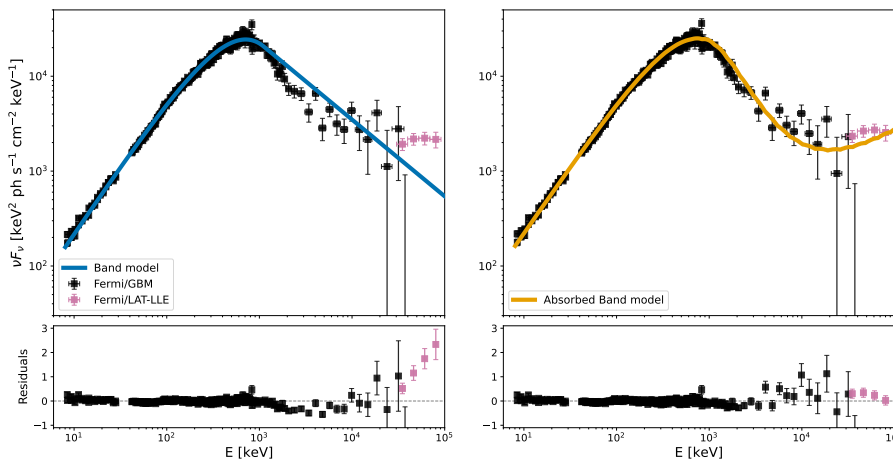


Fig. 2. Comparison between the Band model (left-hand panel) and the absorbed Band model (right-hand panel) applied to the early prompt emission spectrum of GRB 190114C (0-4.15 s).

sorption feature – whether a saddle-like or an exponential cutoff – depends on the low-energy slope of the MeV pulse and on the position of the characteristic energy. Several observed spectral features could naturally arise in this scenario.

First, the characteristic spectral peak of GRBs rarely exceeds ~ 1 MeV (Gruber et al. 2014)². Second, the MeV absorption tends to sharpen the overall width of the observed spectrum, potentially alleviating the long-standing difficulty of reproducing GRB spectra with simple non-thermal emission models.

Interestingly, the fixed threshold for MeV absorption, corresponding to $\sim 2.5 m_e c^2$ in the rest frame, implies a strong redshift dependence of the observed spectral shape. A high-redshift GRB would therefore display the MeV dip or cutoff feature shifted into the hard X-ray band ($\gtrsim 100$ keV). Then, in principle, the identification of this absorption feature can be used as a redshift indicator.

5. Conclusions

We have presented a simple model describing the absorption of MeV γ -rays caused by backscattering of GRB photons in a cold circum-burst medium. When applied to the prompt emission spectrum of GRB 190114C, the model provides a significantly better fit than the standard Band function.

A noticeable MeV absorption requires high progenitor mass-loss rates, $\dot{M} \sim 10^{-4} \text{--} 10^{-1} M_\odot \text{ yr}^{-1}$, which could plausibly occur during enhanced wind episodes in the years preceding core collapse. The detailed shape of the MeV absorption feature depends sensitively on the low-energy spectral slope of the MeV pulse, while the absorption threshold at $\approx 2.5 m_e c^2$ (rest frame) introduces a strong redshift dependence in the observed spectra.

If the circumburst wind density is sufficiently high, this mechanism could account for some common properties of GRB spectra: (i) the characteristic spectral peaks rarely exceed ~ 1 MeV in the rest frame, and (ii) the relatively sharp spectral shapes near the peak energy, which are sometimes difficult to reproduce with standard non-thermal emission models in optically thin jet regions.

Acknowledgements. We thank P. Blasi, E. Kammoun, A. Romagnolo, S. Boula and F. Aharonian for fruitful discussions. This research has made use of data obtained through the High Energy Astrophysics Science Archive Research Center Online Service, provided by the NASA/Goddard Space Flight Center, and specifically, this work made use of public Fermi-GBM and Fermi-LAT data. B.B. acknowledges financial support from the Italian Ministry of University and

Research (MUR) for the PRIN grant METE under contract no. 2020KB33TP. M.B. and G.O. acknowledge the ACME project, which has received funding from the European Union’s Horizon Europe Research and Innovation program under Grant Agreement No. 101131928. This work has been funded by the European Union-Next Generation EU, PRIN 2022 RFF M4C21.1 (202298J7KT - PEACE). O.S.S. acknowledges funding from INAF through grant 1.05.23.04.04.

References

Ajello, M., Arimoto, M., Axelsson, M., et al. 2020, ApJ, 890, 9
 Arnaud, K. A. 1996, in Astronomical Society of the Pacific Conference Series, Vol. 101, Astronomical Data Analysis Software and Systems V, ed. G. H. Jacoby & J. Barnes, 17
 Band, D., Matteson, J., Ford, L., et al. 1993, ApJ, 413, 281
 Beloborodov, A. M. 1999, MNRAS, 305, 181
 Beloborodov, A. M. 2002, ApJ, 565, 808
 Beloborodov, A. M. 2005, ApJ, 627, 346
 Beniamini, P., Nava, L., Duran, R. B., & Piran, T. 2015, MNRAS, 454, 1073
 Campana, S., Mangano, V., Blustin, A. J., et al. 2006, Nature, 442, 1008
 Castro-Tirado, A. J., Hu, Y., Fernandez-Garcia, E., et al. 2019, GRB Coordinates Network, 23708, 1
 Chevalier, R. A. & Li, Z.-Y. 1999, ApJ, 520, L29
 Chugai, N. N., Blinnikov, S. I., Cumming, R. J., et al. 2004, MNRAS, 352, 1213
 Chugai, N. N. & Danziger, I. J. 2003, Astronomy Letters, 29, 649
 Derishev, E. & Piran, T. 2019, ApJ, 880, L27
 Ghisellini, G., Ghirlanda, G., Nava, L., & Celotti, A. 2010, MNRAS, 403, 926
 Groh, J. H. 2014, A&A, 572, L11
 Gruber, D., Goldstein, A., Weller von Ahlefeld, V., et al. 2014, ApJS, 211, 12
 Guilbert, P. W., Fabian, A. C., & Rees, M. J. 1983, MNRAS, 205, 593
 Jauch, J. M. & Rohrlich, F. 1976, The theory of photons and electrons. The relativistic quantum field theory of charged particles with spin one-half (Springer-Verlag, Berlin Heidelberg New York)
 Khazov, D., Yaron, O., Gal-Yam, A., et al. 2016, ApJ, 818, 3
 Kiewe, M., Gal-Yam, A., Arcavi, I., et al. 2012, ApJ, 744, 10
 Kumar, P. & Panaitescu, A. 2004, MNRAS, 354, 252
 Macera, S., Banerjee, B., Mei, A., et al. 2025, A&A, 700, A88
 Madau, P. & Thompson, C. 2000, ApJ, 534, 239
 MAGIC Collaboration, Acciari, V. A., Ansoldi, S., et al. 2019, Nature, 575, 459
 Mészáros, P., Ramirez-Ruiz, E., & Rees, M. J. 2001, ApJ, 554, 660
 Mészáros, P. & Rees, M. J. 1997, ApJ, 476, 232
 Nava, L., Sironi, L., Ghisellini, G., Celotti, A., & Ghirlanda, G. 2013, MNRAS, 433, 2107
 Ofek, E. O., Sullivan, M., Shaviv, N. J., et al. 2014, ApJ, 789, 104
 Oganesy, N., Nava, L., Ghirlanda, G., & Celotti, A. 2017, ApJ, 846, 137
 Panaitescu, A. & Kumar, P. 2002, ApJ, 571, 779
 Pastorello, A., Smartt, S. J., Mattila, S., et al. 2007, Nature, 447, 829
 Pauli, D., Oskinova, L. M., Hamann, W.-R., et al. 2025, A&A, 697, A114
 Planck Collaboration, Ade, P. A. R., Aghanim, N., et al. 2016, A&A, 594, A13
 Ramirez-Ruiz, E., Nishikawa, K.-I., & Hededal, C. B. 2007, ApJ, 671, 1877
 Ravasio, M. E., Ghirlanda, G., Nava, L., & Ghisellini, G. 2019a, A&A, 625, A60
 Ravasio, M. E., Oganesy, G., Ghirlanda, G., et al. 2018, A&A, 613, A16
 Ravasio, M. E., Oganesy, G., Salafia, O. S., et al. 2019b, A&A, 626, A12
 Salafia, O., Celotti, A., Sobacchi, E., et al. 2026, submitted to A&A
 Sander, A. A. C., Lefever, R. R., Pomiątowski, L. G., et al. 2023, A&A, 670, A83
 Schlegel, E. M. 1990, MNRAS, 244, 269
 Svensson, R. 1987, MNRAS, 227, 403
 Thompson, C. & Madau, P. 2000, ApJ, 538, 105
 Tiwari, P., Banerjee, B., Miceli, D., et al. 2025, arXiv e-prints, arXiv:2510.05239
 Toffano, M., Ghirlanda, G., Nava, L., et al. 2021, A&A, 652, A123
 Vink, J. S. & de Koter, A. 2005, A&A, 442, 587
 Vink, J. S., Muijres, L. E., Anthonisse, B., et al. 2011, A&A, 531, A132
 Woosley, S. E. 1993, ApJ, 405, 273
 Woosley, S. E. & Bloom, J. S. 2006, Annual Review of Astronomy and Astrophysics, 44, 507
 Yaron, O., Perley, D. A., Gal-Yam, A., et al. 2017, Nature Physics, 13, 510

² The exact value of the spectral peak depends on the spectral model adopted in the fit.

Appendix A: The MeV absorption model

Here we provide the details of our model for $\gamma-\gamma$ absorption of MeV photons. We assume that the photons have already escaped the jet and neglect its finite angular size, treating the photon injection as one-directional.

Appendix A.1: Single electron in the field of incident photons

A single cold electron (or positron) in an un-perturbed external medium scatters the incoming photons at an average rate (per unit scattered photon energy ε_{sc} – in units of $m_e c^2$ – and unit solid angle at a scattering cosine angle $\mu = \cos \theta$)

$$\frac{dN_{\text{sc}}}{dt d\varepsilon_{\text{sc}} d\Omega}(\varepsilon_{\text{sc}}, \mu) = \int \frac{d\sigma_{\text{KN}}}{d\Omega}(\varepsilon, \mu) \frac{dn_\gamma}{d\varepsilon} c \delta(\varepsilon_{\text{sc}} - \varepsilon/(1 + (1 - \mu)\varepsilon)) d\varepsilon, \quad (\text{A.1})$$

where ε is the energy of the incident photon, $d\sigma_{\text{KN}}/d\Omega$ is the differential Klein-Nishina cross-section, and

$$\frac{dn_\gamma}{d\varepsilon} = \frac{L_e}{4\pi R^2 m_e c^3 \varepsilon}, \quad (\text{A.2})$$

is the specific number density of the incident photons. Here R represents the distance from the central engine where the scattering takes place, $L_e = dL/d\varepsilon$ the specific luminosity of the incident photons, and $\varepsilon/(1 + (1 - \mu)\varepsilon)$ the energy of the scattered photon. A simple transformation of the Dirac delta function

$$\delta(\varepsilon_{\text{sc}} - \varepsilon/(1 + (1 - \mu)\varepsilon)) = \frac{\delta(\varepsilon - \varepsilon_0)}{(1 - (1 - \mu)\varepsilon_{\text{sc}})^2}, \quad (\text{A.3})$$

where

$$\varepsilon_0 = \frac{\varepsilon_{\text{sc}}}{1 - (1 - \mu)\varepsilon_{\text{sc}}}, \quad (\text{A.4})$$

leads to the final expression for the single-electron scattering rate as a function of the incident spectrum,

$$\frac{dN_{\text{sc}}}{dt d\varepsilon_{\text{sc}} d\Omega} = \frac{d\sigma_{\text{KN}}}{d\Omega}(\varepsilon_0, \mu) \cdot \frac{L_e(\varepsilon_0)}{4\pi R^2 m_e c^2} \cdot \frac{1}{\varepsilon_{\text{sc}} [1 - (1 - \mu)\varepsilon_{\text{sc}}]}. \quad (\text{A.5})$$

Appendix A.2: Propagation of the scattered photons

A scattered photon of energy ε_{sc} and scattering angle μ can undergo $\gamma - \gamma$ absorption when interacting with another incident photon. The mean free path of the scattered photon due to such absorption process can be defined as

$$\lambda_{\gamma\gamma}^{-1}(\varepsilon_{\text{sc}}, \mu) = \int_{\varepsilon_{\text{th}}}^{+\infty} (1 - \mu) \sigma_{\gamma\gamma}(\varepsilon_{\text{sc}}, \varepsilon, \mu) \frac{dn_\gamma}{d\varepsilon} d\varepsilon, \quad (\text{A.6})$$

where ε represents again the energy of an incident photon, $\varepsilon_{\text{th}} = 2/(1 - \mu)\varepsilon_{\text{sc}}$ is the threshold for $\gamma - \gamma$ absorption, and

$$\sigma_{\gamma\gamma}(\varepsilon_{\text{sc}}, \varepsilon, \mu) = \frac{3\sigma_T}{8x^2} \left[(2 + 2x^{-2} - x^{-4}) \ln(x + \sqrt{x^2 - 1}) - (1 + x^{-2}) \sqrt{1 - x^{-2}} \right], \quad (\text{A.7})$$

is the Breit-Wheeler cross section, with $x = \sqrt{\varepsilon_{\text{sc}}\varepsilon(1 - \mu)/2}$ (Jauch & Rohrlich 1976).

A good approximation of $\lambda_{\gamma\gamma}$ can be obtained by approximating $\sigma_{\gamma\gamma}$ as a delta function centered at $\varepsilon = 2\varepsilon_{\text{th}} = 4/(1 - \mu)\varepsilon_{\text{sc}}$ (i.e. where the cross section is maximised), with a normalization $\sigma_{\gamma\gamma} \sim \eta\sigma_T\delta(\varepsilon - 2\varepsilon_{\text{th}})$ that is set by a constant η (e.g. Svensson 1987). This results in

$$\lambda_{\gamma\gamma}^{-1}(\varepsilon_{\text{sc}}, \mu) \sim \frac{L_e \left(\frac{4}{(1 - \mu)\varepsilon_{\text{sc}}} \right) \eta\sigma_T(1 - \mu)}{4\pi R^2 m_e c^3}, \quad (\text{A.8})$$

As shown in Fig. A.1, for our assumed incident spectrum this approximation is quite accurate when setting $\eta \approx 0.35$. In our implementation, we make use of this approximation when computing $\lambda_{\gamma\gamma}$ for the scattered photons. Conversely, we use the exact formula when computing the $\gamma - \gamma$ optical depth for incident photons, because this affects the detailed shape of the absorbed spectrum.

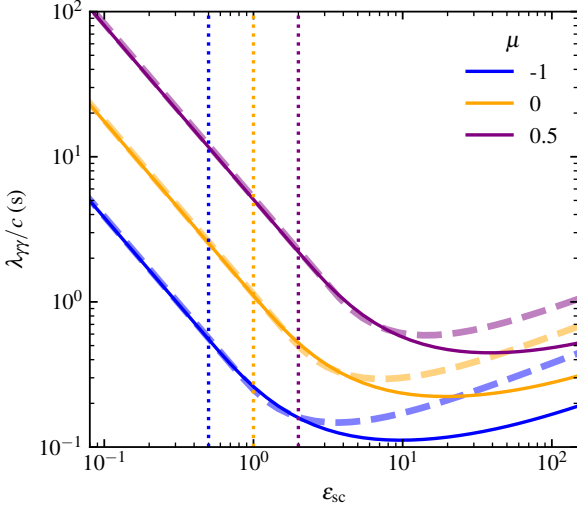


Fig. A.1. Exact and approximate $\gamma - \gamma$ absorption mean free path. Solid lines show the exact $\gamma - \gamma$ absorption mean free path (Eq. A.6) of a photon with energy ε_{sc} scattered at a radius $R_0 = 10^{16}$ cm to a cosine angle μ (different colors refer to different values of μ as given in the legend) moving through an incident radiation with $L = 10^{53}$ erg/s, $E_p = 1$ MeV, $\alpha = -0.6$ and $\beta = -2.2$. Dashed lines show the corresponding approximate mean free path (Eq. A.8) setting $\eta = 0.35$. Each dotted line shows the maximum energy of a scattered photon whose scattering angle μ is given by the corresponding color in the legend.

Appendix A.3: Absorption of incident photons

Let us now indicate with $t = 0$ the time when the first incident photon reaches the radius R of interest. At a later time t , the average number density of scattered photons (per unit solid angle and per unit energy of the scattered photon ε_{sc}) is obtained³ by summing over all photons scattered at times $0 < t_{\text{sc}} < t$, and accounting for the fact that only a fraction $e^{-c(t-t_{\text{sc}})/\lambda_{\gamma\gamma}}$ has survived to $\gamma - \gamma$ absorption, namely

$$\frac{dn_{\gamma}}{d\varepsilon_{\text{sc}} d\Omega}(R, \varepsilon_{\text{sc}}, \mu, t) \sim \int_0^t \hat{n}(R, t_{\text{sc}}) \frac{dN_{\text{sc}}}{dt d\varepsilon_{\text{sc}} d\Omega}(\varepsilon_{\text{sc}}, \mu) e^{-\frac{c(t-t_{\text{sc}})}{\lambda_{\gamma\gamma}(\varepsilon_{\text{sc}}, \mu)}} dt_{\text{sc}}. \quad (\text{A.9})$$

Here $\hat{n}(R, t_{\text{sc}})$ is the lepton number density of the medium at time t_{sc} . This includes both the original electrons and the pairs created during the process. Under the assumption that the incident spectrum is constant, and in a case where the lepton number density remains constant with time (so that $\hat{n}(R, t_{\text{sc}}) \sim \hat{n}(R, 0) = \hat{n}(R)$, i.e. the pair enrichment is negligible) we can simplify the above expression as

$$\frac{dn_{\gamma}}{d\varepsilon_{\text{sc}} d\Omega}(R, \varepsilon_{\text{sc}}, \mu, t) \sim \hat{n}(R) \frac{dN_s}{dt d\varepsilon_{\text{sc}} d\Omega}(\varepsilon_{\text{sc}}, \mu) \frac{\lambda_{\gamma\gamma}(\varepsilon_{\text{sc}}, \mu)}{c} \delta\hat{t}(\varepsilon_{\text{sc}}, \mu, t), \quad (\text{A.10})$$

where

$$\delta\hat{t}(\varepsilon_{\text{sc}}, \mu, t) = 1 - e^{-\frac{ct}{\lambda_{\gamma\gamma}(\varepsilon_{\text{sc}}, \mu)}}. \quad (\text{A.11})$$

This shows that, at time t , the photon density is essentially set by photons scattered during a time interval preceding t of duration $\lambda_{\gamma\gamma}\delta\hat{t}(\varepsilon_{\text{sc}}, \mu)/c \leq \lambda_{\gamma\gamma}/c$, because photons scattered at earlier times have entirely annihilated by then. We call this the ‘survival time’ of scattered photons. In Fig. A.2 we show examples of $\delta\hat{t}$ and the corresponding single-scattering spectrum.

The above result also implies that, even in a case where the lepton density \hat{n} evolves over time (because of pair enrichment), the scattered photon density only depends on an appropriately averaged density of the leptons over the latest $\lambda_{\gamma\gamma}/c$ time. Alternatively, the evolution of \hat{n} can be seen as an additional factor that modifies the survival time $\delta\hat{t}$ into a new, effective one $\delta\hat{t}_{\text{eff}}$. This can be seen by writing the lepton density in Eq. A.9 as $\hat{n}(R, t_{\text{sc}}) = \hat{n}(R, 0) \times (\hat{n}(R, t_{\text{sc}})/\hat{n}(R, 0))$, which leads to

$$\frac{dn_{\gamma}}{d\varepsilon_{\text{sc}} d\Omega}(R, \varepsilon_{\text{sc}}, \mu, t) \approx \hat{n}(R, 0) \frac{dN_{\text{sc}}}{dt d\varepsilon_{\text{sc}} d\Omega}(\varepsilon_{\text{sc}}, \mu) \int_0^t \frac{\hat{n}(R, t_{\text{sc}})}{\hat{n}(R, 0)} e^{-\frac{c(t-t_{\text{sc}})}{\lambda_{\gamma\gamma}(\varepsilon_{\text{sc}}, \mu)}} dt_{\text{sc}} \equiv \hat{n}(R, 0) \frac{dN_{\text{sc}}}{dt d\varepsilon_{\text{sc}} d\Omega}(\varepsilon_{\text{sc}}, \mu) \frac{\lambda_{\gamma\gamma}(\varepsilon_{\text{sc}}, \mu)}{c} \delta\hat{t}_{\text{eff}}(\varepsilon_{\text{sc}}, \mu), \quad (\text{A.12})$$

with

$$\delta\hat{t}_{\text{eff}}(\varepsilon_{\text{sc}}, \mu) = \int_0^t \frac{\hat{n}(R, t)}{\hat{n}(R, 0)} e^{-\frac{c(t-t_{\text{sc}})}{\lambda_{\gamma\gamma}(\varepsilon_{\text{sc}}, \mu)}} d\frac{ct_{\text{sc}}}{\lambda_{\gamma\gamma}} = e^{-ct/\lambda_{\gamma\gamma}} \int_0^{ct/\lambda_{\gamma\gamma}} \frac{\hat{n}(R, x\lambda_{\gamma\gamma}/c)}{\hat{n}(R, 0)} e^x dx. \quad (\text{A.13})$$

It is straightforward to see that the above equation reduces to Eq. A.11 in the case of a constant lepton density.

The differential optical depth to $\gamma - \gamma$ absorption for an incident photon travelling at time t through the field of photons previously scattered by material located within $(R, R + dR)$ is

$$\frac{d\tau_{\gamma\gamma}}{dR}(\varepsilon, R, t) = 2\pi \int_{-1}^1 \int_{\varepsilon_{\text{th}, \text{sc}}}^{+\infty} \frac{dn_{\gamma}}{d\varepsilon_{\text{sc}} d\Omega}(\varepsilon_{\text{sc}}, \mu, t) (1-\mu) \sigma_{\gamma\gamma}(\varepsilon, \varepsilon_{\text{sc}}, \mu) d\varepsilon_{\text{sc}} d\mu = 2\pi \int_{-1}^1 \int_{\varepsilon_{\text{th}, \text{sc}}}^{+\infty} \frac{dn_{\gamma}}{d\varepsilon_{\text{sc}} d\Omega}(\varepsilon_{\text{sc}}, \mu, t) (1-\mu) \sigma_{\gamma\gamma}(\varepsilon, \varepsilon_{\text{sc}}, \mu) d\varepsilon_{\text{sc}} d\mu,$$

³ Because all the process happens in a time less than r/c , scattered photons can be assumed to remain close to their scattering centres.

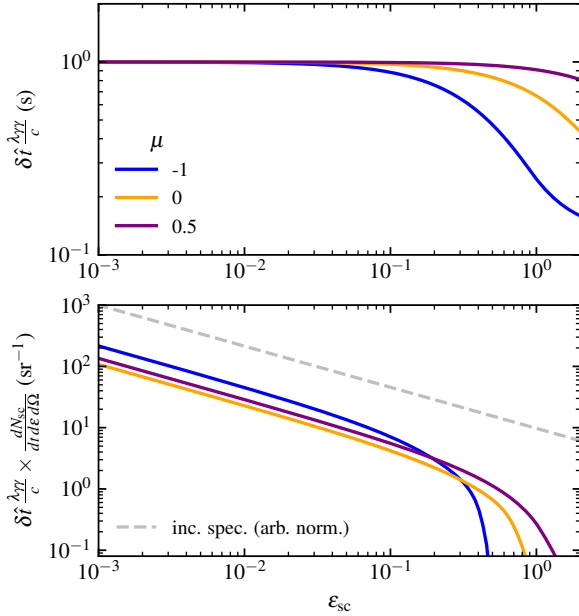


Fig. A.2. Scattered photon survival time and corresponding spectrum. We have assumed $t_0 = 1$ s, $\alpha = -2/3$, $\beta = -2.2$, $E_p = 1$ MeV, $L = 10^{53}$ erg/s and $R = 10^{16}$ cm. The solid lines in the top panel show the survival time of scattered photons with three different scattering angles (given in the legend) before they completely annihilate with incident photons. Lines with the same colors in the bottom panel show the corresponding spectrum of these scattered photons, expressed as the product of the survival time and the specific scattering rate. The grey dashed line shows the incident spectrum, arbitrarily normalized, for comparison.

(A.14)

where $\varepsilon_{\text{th,sc}} = 2/(1-\mu)\varepsilon$ is the threshold scattered photon energy for it to cause $\gamma-\gamma$ absorption of the incident photon. As discussed in the main text, in our scenario most of the optical depth at time t is provided by scattering close to a specific radius $R = R_0(t)$. Under the assumption of a wind-like external profile, so that $\hat{n}(R, 0) = \hat{A}R^{-2}$, and using approximation A.8 for $\lambda_{\gamma\gamma}$, we can then write the total optical depth as

$$\tau_{\gamma\gamma}(\varepsilon, t) \sim R_0 \frac{d\tau_{\gamma\gamma}}{dR}(R_0) \sim \frac{2\pi\hat{A}}{R_0} \int_{-1}^1 \int_{\frac{2}{(1-\mu)\varepsilon}}^{+\infty} \frac{d\sigma_{\text{KN}}}{d\Omega}(\varepsilon_0, \mu) \frac{L_\varepsilon(\varepsilon_0)}{L_\varepsilon(2\varepsilon_{\text{th}})} \frac{\sigma_{\gamma\gamma}(\varepsilon, \varepsilon_{\text{sc}}, \mu)}{\eta\sigma_T} \frac{\delta\hat{t}_{\text{eff}}(\varepsilon_{\text{sc}}, \mu)}{\varepsilon_{\text{sc}} [1 - (1-\mu)\varepsilon_{\text{sc}}]} d\varepsilon_{\text{sc}} d\mu, \quad (\text{A.15})$$

where again $\varepsilon_0 = \varepsilon_{\text{sc}}/(1 - (1-\mu)\varepsilon_{\text{sc}})$ and $2\varepsilon_{\text{th}} = 4/(1-\mu)\varepsilon_{\text{sc}}$.

For a very high column density \hat{A}/R_0 , Thompson scattering can further affect the low-energy spectrum, thus the overall optical depth is $\tau(\varepsilon) \approx \tau_{\text{ye}}(\varepsilon) + \tau_{\gamma\gamma}(\varepsilon)$ where $\tau_{\text{ye}}(\varepsilon) \sim \frac{\hat{A}}{R_0} \sigma_{\text{KN}}(\varepsilon)$ and $\sigma_{\text{KN}}(\varepsilon)$ is the total Klein-Nishina cross section.

Appendix A.4: Pair-enriched medium

The electron-positron pairs produced by the annihilation of the scattered X-ray radiation amplifies the density of leptons (Madau & Thompson 2000). Before the deposition of momentum into the outer medium by scattering and pair production becomes significant, the lepton density amplification factor can be written as (Beloborodov 2002)

$$\frac{\hat{n}(R, t_{\text{sc}})}{\hat{n}(R, 0)} = \frac{1}{2} (e^{\xi(R, t_{\text{sc}})/\xi_{\text{load}}} + e^{-\xi(R, t_{\text{sc}})/\xi_{\text{load}}}), \quad (\text{A.16})$$

where $\xi(R, t_{\text{sc}}) = ct_{\text{sc}}/\lambda_{\text{ey}}$ is a dimensionless time coordinate, $\lambda_{\text{ey}} \approx 4\pi R^2 m_e c^3 / L \sigma_T$ is the mean free path of an electron in the field of incident photons, and $\xi_{\text{load}}(E_p, \alpha, \beta) \sim 20 - 30$ is the characteristic pair-enrichment scale which depends on the spectral shape (set by E_p , α and β) of the incident photons⁴. The exponential growth of pairs effectively continues until $\xi_{\text{acc}} \approx 5\xi_{\text{load}}$ (assuming an external medium composed primarily of hydrogen), after which the medium accelerates to ultra-relativistic velocities. Once the pair-enriched layer of the medium is ultra-relativistic, the pair-loading gets suppressed and the MeV absorption rapidly shifts to higher photon energies. The absorption effects discussed in this work are therefore relevant at scattering times $t_{\text{sc}} \leq t_{\text{acc}}$, where $t_{\text{acc}} = \xi_{\text{acc}} \lambda_{\text{ey}}/c$. At later times, for simplicity, we approximate the effect of the radiative acceleration of the external medium simply as a cut-off in the external density, $\hat{n}(R, t_{\text{sc}} > t_{\text{acc}}) = 0$, but we stress that these times are not of interest for our investigation: when radiative acceleration is important at a radius R (and hence absorption is suppressed), then the relevant radius for absorption will shift to a larger radius $R_0 > R$ for which the acceleration has not become effective yet. Such radius can be estimated by setting $\xi_{\text{acc}} = ct/\lambda_{\text{ey}}$, which yields

$$R_0(t) \sim \left(\frac{\sigma_T L t}{4\pi m_e c^2 \xi_{\text{acc}}} \right)^{1/2} \approx 7.9 \times 10^{15} L_{53}^{1/2} t_0^{1/2} \xi_{\text{acc}, 2}^{-1/2} \text{ cm}. \quad (\text{A.17})$$

⁴ Beloborodov (2005) derived a formula for ξ_{load} that depends on α and β only, assuming that $E_p = 511$ keV, while no general formula exists yet to our knowledge. In this work, we set $\xi_{\text{load}} = 20$ for simplicity, since the expected range of variation of this parameter is small and does not dominate our systematics. We note that this also sets $\xi_{\text{acc}} \approx 5\xi_{\text{load}} \approx 100$.

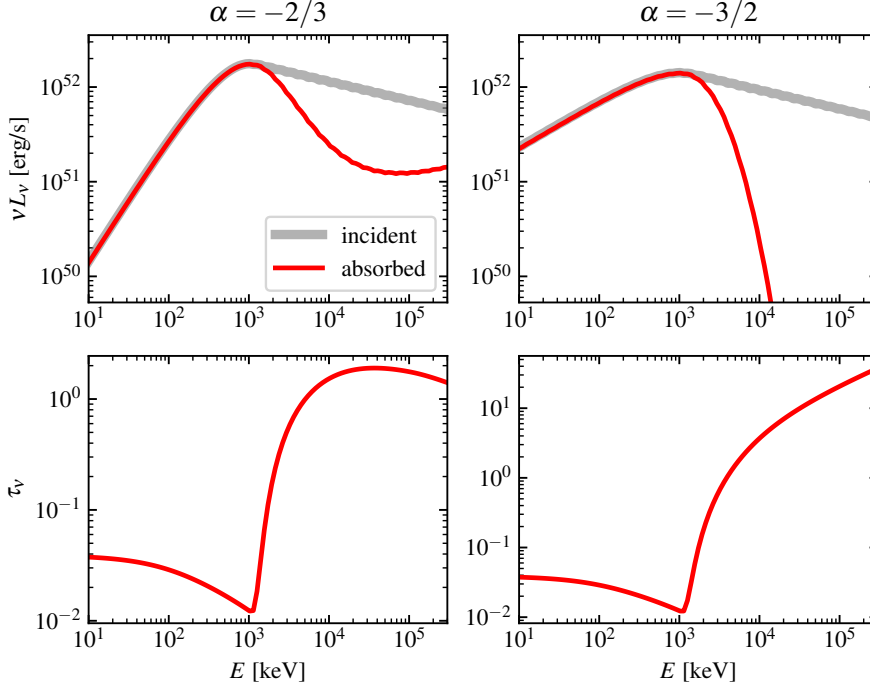


Fig. A.3. Example incident and absorbed spectra and corresponding optical depth for incident photons. Incident spectra (grey solid lines) are characterised by $\beta = -2.2$, $E_p = 1$ MeV, $L = 10^{33}$ erg/s, and a low-energy photon index $\alpha = -2/3$ (left-hand panels, representative of synchrotron in marginally fast cooling) or $\alpha = -3/2$ (right-hand panels, for synchrotron in fast cooling). The absorbed spectra, assuming $t = 1$ s (which implies $R_0 = 7.9 \times 10^{15}$ cm) and $A_\star = 10^3$ cm $^{-3}$, are shown with red lines in the top panels. The corresponding optical depth, which includes both Thomson scattering and $\gamma - \gamma$ absorption, is shown in the bottom panels. For $\alpha = -2/3$, the absorption feature is saddle-shaped, while for $\alpha = -3/2$ it produces a spectral cut-off.

For a given choice of t , radii $R \ll R_0$ do not contribute significantly to the absorption because they have been radiatively accelerated; larger radii $R \gg R_0$ do not contribute significantly because they are less dense (assuming a wind-like density profile) and because they are less pair-enriched. Hence, most of the absorption happens around $R = R_0(t)$.

That said, the effective time $\delta\hat{t}_{\text{eff}}(\varepsilon_{\text{sc}}, \mu)$ in the pair-enriched medium case, from Eq. A.13, is

$$\delta\hat{t}_{\text{eff}}(\varepsilon_{\text{sc}}, \mu, t) = \frac{1}{2} \int_0^{\min(t, t_{\text{acc}})} \left(e^{\frac{ct}{\lambda_{\text{ey}}\xi_{\text{load}}} + \mu} + e^{-\frac{ct}{\lambda_{\text{ey}}\xi_{\text{load}}}} \right) e^{-\frac{c}{\lambda_{\gamma\gamma}(\varepsilon, \mu)}(t-t_{\text{sc}})} \frac{c}{\lambda_{\gamma\gamma}} dt_{\text{sc}} = \frac{e^{-ct/\lambda_{\gamma\gamma}}}{2} \int_0^{\min(t, t_{\text{acc}})c/\lambda_{\gamma\gamma}} \left(e^{\frac{\lambda_{\gamma\gamma}}{\lambda_{\text{ey}}\xi_{\text{load}}}x + \mu} + e^{-\frac{\lambda_{\gamma\gamma}}{\lambda_{\text{ey}}\xi_{\text{load}}}x} \right) e^x dx. \quad (\text{A.18})$$

The integral is analytical and it formally results in

$$\delta\hat{t}_{\text{eff}}(\varepsilon_{\text{sc}}, \mu, t) = \frac{e^{-ct/\lambda_{\gamma\gamma}}}{2} \left(\frac{e^{(1+\rho_{\text{acc}})c \min(t, t_{\text{acc}})/\lambda_{\gamma\gamma}}}{1 + \rho_{\text{acc}}} + \frac{e^{(1-\rho_{\text{acc}})c \min(t, t_{\text{acc}})/\lambda_{\gamma\gamma}}}{1 - \rho_{\text{acc}}} - \frac{2}{1 - \rho_{\text{acc}}^2} \right), \quad (\text{A.19})$$

where

$$\rho_{\text{acc}}(\varepsilon_{\text{sc}}, \mu) = \frac{\lambda_{\gamma\gamma}(\varepsilon_{\text{sc}}, \mu)}{\xi_{\text{load}}\lambda_{\text{ey}}} \approx \frac{L}{\xi_{\text{load}}L_{\text{e}}\left(\frac{4}{(1-\mu)\varepsilon_{\text{sc}}}\right)\eta(1-\mu)}. \quad (\text{A.20})$$

When $R = R_0$, we have $t = t_{\text{acc}}$ and $\xi = \xi_{\text{acc}} \approx 5\xi_{\text{load}}$, therefore the above expression simplifies to

$$\delta\hat{t}_{\text{eff}}(\varepsilon_{\text{sc}}, \mu, t) = \frac{1}{2} \left(\frac{e^{(1+\rho_{\text{acc}})}}{1 + \rho_{\text{acc}}} + \frac{e^{(1-\rho_{\text{acc}})}}{1 - \rho_{\text{acc}}} - \frac{2e^{-5\xi_{\text{load}}}}{1 - \rho_{\text{acc}}^2} \right), \quad (\text{A.21})$$

which is the expression that we use in our model.

The optical depth due to the Thompson scattering is simply

$$\tau_{\text{ye}}^\pm(\varepsilon, t) \sim \frac{\hat{A}}{2R_0} \sigma_{\text{KN}}(\varepsilon) (e^{\xi(R_0, t)/\xi_{\text{load}}} + e^{-\xi(R_0, t)/\xi_{\text{load}}}) \sim \frac{\hat{A}}{2R_0} \sigma_{\text{KN}}(\varepsilon) (e^{\xi_{\text{acc}}/\xi_{\text{load}}} + e^{-\xi_{\text{acc}}/\xi_{\text{load}}}) \approx \frac{74\hat{A}}{R_0} \sigma_{\text{KN}}(\varepsilon) \approx 1.5 A_{\star, 2} R_{0, 15}^{-1} \frac{\sigma_{\text{KN}}(\varepsilon)}{\sigma_{\text{T}}}, \quad (\text{A.22})$$

where the last three expressions assume that $\xi = \xi_{\text{acc}}$.

Figure A.3 shows example incident and absorbed spectra calculated with our model for a particular choice of model parameters, highlighting the effect of assuming two different low-energy photon indices for the incident spectrum. The bottom panels show the total optical depth, which is dominated by Thomson scattering below 1 MeV and by $\gamma - \gamma$ absorption above. When the low-energy photon index is harder than -1, as expected in a marginally-fast-cooling synchrotron scenario (Oganesyan et al. 2017) the absorption feature has a ‘saddle’ shape; if the incident spectrum is softer, as expected in the usual fast-cooling synchrotron scenario, then the absorption induces a spectral cut-off.

Appendix B: GRB 190114C fit results

We report in Table B.1 the results of fitting two spectral models to the *Fermi* observations of GRB 190114C during the first 4.15 s after the *Fermi*/GBM trigger. The models are either Band, or a model where the incident spectrum is still described by the Band function, but the effect of our absorption process is taken into account. More details are given in the main text.

Table B.1. Best fit parameters for the Band and absorbed Band models.

Parameter	Value
Band model	
α	-0.558 ± 0.009
β	-2.81 ± 0.03
$E_p/(1+z)$ [keV]	709^{+16}_{-13}
norm [ph cm $^{-2}$ s $^{-1}$ keV $^{-1}$]	$0.6105^{+0.005}_{-0.006}$
Stat/dof	803/350
Absorbed Band model	
α	-0.59 ± 0.01
β	$-2.03^{+0.03}_{-0.08}$
$\log_{10}(E_p/\text{keV})$	3.01 ± 0.01
$\log_{10}(L/\text{erg s}^{-1})$	$53.55^{+0.06}_{-0.12}$
$\log_{10}(\hat{A}_\star/\text{cm}^{-3})$	$3.98^{+0.11}_{-0.22}$
$\log_{10}(R_0/\text{cm})^\dagger$	$16.40^{+0.03}_{-0.05}$
Stat/dof	656/349

^(\dagger) Derived parameter, computed through Eq. 6.